ANALYSIS OF LINEAR AEROSPIKE PLUME INDUCED X-33 BASE-HEATING ENVIRONMENT

Ten-See Wang*

NASA Marshall Space Flight Center, Huntsville, AL 35812

Computational analysis is conducted to study the effect of an linear aerospike engine plume on the X-33 base-heating environment during ascent flight. To properly account for the freestream-body interaction and to allow for potential plume-induced flow-separation, the thermo-flowfield of the entire vehicle at several trajectory points is computed. A sequential grid-refinement technique is used in conjunction with solution-adaptive, patched, and embedded grid methods to limit the model to a manageable size. The computational methodology is based on a three-dimensional, finite-difference, viscous flow, chemically reacting, pressure-based computational fluid dynamics formulation, and a three-dimensional, finite-volume, spectral-line based weighted-sum-of-gray-gases absorption, computational radiation heat transfer formulation. The computed forebody and afterbody surface pressure coefficients and base pressure characteristic curves are compared with those of a cold-flow test. The predicted

---

Presented as paper 98-2469 at the 7th AIAA/ASME Joint Thermophysics and Heat Transfer Conference, Albuquerque, NM, June 15-18, 1998. Copyright © 1998 by the American Institute of Aeronautics and Astronautics, Inc. No copyright is asserted in the United States under Title 17, U.S. Code. The U.S. Government has a royalty-free license to exercise all rights under the copyright claimed herein for Governmental purposes. All other rights are reserved by the copyright owner.

* Team Leader, Fluid Dynamics Analysis Branch, Senior Member AIAA.

convective and radiative base-heat fluxes, the effect of base-bleed, and the potential of plume-induced flow separation are presented.

Nomenclature

C_p = pressure coefficient

C_1,C_2,C_3,C_μ= turbulence modeling constants, 1.15, 1.9, 0.25, and 0.09.

G = geometrical metrices

H = total enthalpy

h = static enthalpy or altitude, km

I = radiative intensity

J = Jacobian of coordinate transformation

k = turbulent kinetic energy

M = mach number

N = total number of chemical species

NPR = chamber to ambient pressure ratio

P = pressure

PC = combustion chamber pressure

Pr = Prandtl number

Q = heat flux, kW/m^2

q = 1, u, v, w, H, k, ε, or ρ_i

R = recovery factor

S_q = source term for equation q

T^+ = nondimensional temperature

t = time

U = volume-weighted contravariant velocity

u, v, w = mean velocities in three directions

u_τ = wall friction velocity

u^+ = nondimensional velocity, (u/u_τ)

y^+ = nondimensional distance, $(y_p u_\tau \rho/\mu)$

ε = turbulent kinetic energy dissipation rate or wall emissivity

κ = absorption coefficient

μ = effective viscosity, $(\mu_l + \mu_t)$

ξ = computational coordiantes

Π = turbulent kinetic energy production

ρ = density

σ_q = turbulence modeling constants

φ = energy dissipation function

Ω = direction vector

ω = chemical species production rate

Subscripts

a = ambient

b = black body or base

c = convective or center

l = laminar flow

p = off-wall (wall function) point

r = radiative

t = turbulent flow

w = wall surface

∞ = freestream

Introduction

In 1996, Lockheed Martin Skunk Works was selected to build and fly the wedge-shaped X-33 Advanced Technology Demonstrator for NASA's Reusable Launch Vehicle (RLV) program. The X-33 is a half-scale prototype of a rocket-based single-stage-to-orbit system, which will ultimately be the next-generation RLV. The X-33 is fueled by liquid hydrogen/liquid oxygen, and features a lifting body configuration coupled with two integrated, linear aerospike rocket engines to propel the vehicle.

It is well known that aerospike engines have the potential advantage of adjusting themselves to perform with maximum efficiency at all altitudes.[1-2] However, the heating effect of the hot combustion chamber gases shooting along the exposed ramp surface on the vehicle base components is less known. In order to properly design the thermal protection system for the base components, accurate accounting of a unified thermo-flowfield around the base region is required. In this study, as part of an integrated effort, a computational methodology is developed and calculations are performed to provide a plume-induced base-heating environment for the X-33 thermal protection system design effort.

Solution Methodology

Computational Grid Generation

A sequential grid-refinement technique is used in this study. That is, the flow solution is initially obtained on a baseline grid, then upgraded with solution-adaptive, patched, and embedded grid methods in a sequential fashion. Figure 1 shows the layout of an X-33 surface computational grid. In actual calculations, only 1/2 of the domain is used assuming flow symmetry. A 22-zone, 1,803,614-point baseline grid is generated first, using the software package GRIDGEN.[3] It is anticipated, however, that the general topology of the baseline grid may not allow efficient capturing of certain flow physics such as shocks. A Self-Adaptive Grid codE (SAGEv2)[4] is then used to redistribute the grid. A typical SAGEv2 smoothed grid plane is shown in Fig. 2 in which the nose and plume shocks are adapted. The distance between the base and the grid exit domain is 2.5 times the vehicle-length to ensure enough hot plume volume is considered for base radiative heating calculations. In the beginning, the baseline grid (1,803,614 points) had a coarse grid density for the engine ramp region, a lumped single-thruster inlet (instead of 20-thruster per engine), and a flattened plug-base (which was later redesigned to a pillowed-base configuration). These grid zones were sequentially upgraded to include a refined 20-thruster inlet (grid density increased to 2,131,790 points) and a pillowed plug-base (grid density increased to 2,217,444 points), as shown in Fig. 3. The pillow-shaped base-protrusions have thousands of small bleed holes that release hydrogen gas called base-bleed, to protect the plug-base from the hot plume impingement. A single-thruster solution was run separately and the exit plane solution was mapped individually onto the 20-thruster inlet (as shown in Fig. 3), for the full-vehicle calculations. In general, solution-adapted grid method was used to redistribute the grid topology in the freestream and far-field plume regions; the patched-grid method was used on zonal interfaces where grid-line discontinuity occurred due to solution-adaptive grid distributions or an entire zonal grid replacement (e.g., the refined 20-thruster inlet); and the embedded-grid method was used to perform local grid refinement. An example of an embedded-grid is located on the aftbody surface and between the vertical fins, as shown in Fig. 1. This sequential grid-refinement strategy and the three grid distribution methods allow the full-vehicle base-flow physics to be computed in an efficient manner.

Thermal Environment Computation

Thermal environment solutions about the X-33 base-heating environment are carried out with two computational tools: the Finite-Difference Navier-Stokes (FDNS) CFD code[5] for the convective heating and the General Radiation Solution Program (GRASP)[6] for the radiative heating. These tools were developed at Marshall Space Flight Center (MSFC) and are continuously being improved by MSFC personnel and its supporting contractors. Systematic and rigorous benchmark studies have been performed for base flow and heat transfer applications. For example, FDNS has been validated for convective heat transfer inside rocket thrust chambers[7] and coolant channels[8], for base-pressure characteristic curve of a four-engine clustered nozzle configuration[9-10], for Delta Clipper-Experimental (DC-X) base-drag induced by the engine exhaust during cold flow and flight tests[11], and for DC-X convective base-heat flux during landing[12], whereas GRASP has been benchmarked for DC-X radiative base-heat flux during landing[12]. In this study, FDNS and GRASP calculations are conducted sequentially in order to save computational memory. The solution algorithm for the thermal environment computation is summarized in the following.

Convective Heat Transfer

FDNS solves a general curvilinear coordinate, chemically reacting, viscous thermo-flowfield with Reynolds-averaged transport equations. A generalized form of these equations is given by

$$\frac{\partial \rho q}{J \partial t} = \frac{\partial \left[-\rho U q + \left(\mu / \sigma_q \right) G \left(\partial q / \partial \xi \right) \right]}{\partial \xi} + \frac{S_q}{J} \tag{1}$$

A pressure-based predictor-plus-multicorrector solution method is applied.[13] The basic idea is to perform correction for the pressure and velocity fields by solving for a pressure correction so that the velocity-pressure coupling is enforced, based on the continuity constraint. A second-order central-difference scheme is employed to discretize the diffusion fluxes and source terms of the governing equations. For the convective terms, a second-order total-variation-diminishing difference scheme is used in this effort.

An extended k-ε turbulence model[14] is used to describe the turbulence. $\mu_t = \rho C_\mu k^2/\varepsilon$ is defined as the turbulence eddy viscosity. Turbulence modeling constants σ_q and source terms S_q of the transport equations are given in Table 1. These turbulence modeling constants have been used extensively for combustion driven and base flows[7-13,15], while σ_k and σ_ε are taken from the turbulence closure.[14] A 7-species, 9-reaction detailed mechanism[15] is used to describe the finite-rate hydrogen-oxygen afterburning chemical kinetics. The seven species are H_2, O_2, H_2O, O, H, OH, and N_2, and H_2O is the only radiating medium.

Table 1 σ_q and S_q of the transport equations

q	σ_q	S_q
1	1.00	0
u	1.00	$-P_x+\nabla[\mu(u_j)_x]-(2/3)(\mu\nabla u_j)_x$
v	1.00	$-P_y+\nabla[\mu(u_j)_y]-(2/3)(\mu\nabla u_j)_y$
w	1.00	$-P_z+\nabla[\mu(u_j)_z]-(2/3)(\mu\nabla u_j)_z$
H	0.95	$DP/DT+\varphi$
k	1.00	$\rho(\Pi-\varepsilon)$
ε	1	$\rho(\varepsilon/k)\{[C_1+C_3(\Pi/\varepsilon)]\Pi-C_2\varepsilon\}$
ρ_i	1.00	ω_i, $i = 1,\ldots,N$

A modified wall function approach is employed to provide wall boundary layer solutions that are less sensitive to the near-wall grid spacing. Consequently, the model has combined the advantages of both the integrated-to-the-wall approach and the conventional law-of-the-wall approach by incorporating a complete velocity profile[16] given by

$$u+ = \ln\left[\left(y^+ + 11\right)^{4.02} / \left(y^{+2} - 7.37y^+ + 83.3\right)^{0.79}\right] \\ + 5.63\tan^{-1}\left(0.12y^+ - 0.441\right) - 3.81 \tag{2}$$

and a universal temperature profile[17] given by

$$T^+ = u^+ + 12.8(\mathrm{Pr}_l^{0.68} - 1) \tag{3}$$

The convective heat transfer from a hot boundary layer to a cooler wall follows the modified Newtonian law[12]

$$Q_{cw} = \left(\rho u_\tau / T^+\right)\left[h_w - h_p - R\left(u_p^2/2\right)\right] \tag{4}$$

where $R = \mathrm{Pr}_l^{1/2}$ if $y^+ \leq 11.63$ and $R = \mathrm{Pr}_l^{1/3}$ if $y^+ > 11.63$, and $y^+ = 11.63$ is the thickness of the viscous sublayer. A constant Pr_l of air is used in this study, since parametric studies performed in Ref. 12 show that the H_2/O_2 plume induced base heat flux is not sensitive to a multicomponent variable Pr_l.

Radiative Heat Transfer

GRASP analyzes the radiative field by solving the general curvilinear coordinate radiative transfer equation with a finite-volume method (FVM) formulation:[18]

$$(\Omega \cdot \nabla) I(r,\Omega) = -\kappa I(r,\Omega) + \kappa I_b(r) \tag{5}$$

The term on the left-hand side represents the gradient of the intensity in the direction of Ω. The two terms on the right-hand side represent the changes in intensity due to absorption and emission. The wall boundary is assumed gray while emitting and reflecting diffusely, and the radiative wall boundary condition is given by

$$I(r_w,\Omega^+) = \varepsilon I_b(r_w) + \frac{(1-\varepsilon)}{\pi} \int_{n.\Omega^- < 0} I(r_w,\Omega^-) |n.\Omega^-| d\Omega^- \tag{6}$$

with

$$Q_{rw} = \int_{n.\Omega^- < 0} I(r_w,\Omega^-) |n.\Omega^-| d\Omega^- \tag{7}$$

where Ω^+ and Ω^- denote the leaving and arriving radiative intensity directions, respectively. The 20-band spectral-line weighted-sum-of-gray-gases model[6] is used to calculate the total emissivity and absorptivity of the radiating medium. Following the ray-dependency test performed in Ref. 12, the FVM 6x4 option - six control angles in the polar direction and four in the azimuthal direction - is deemed as adequate and used in this effort.

Boundary and Initial Conditions

The outer boundary of the computational domain is bounded by the fixed total condition (free-stream) boundaries, one symmetry plane, and the flow exit plane (see Fig. 2). A no-slip wall is specified for the body surface. A fixed (ambient) static pressure is imposed on the exit plane and on a point far away from the action area (one grid point off the freestream boundary), in order to obtain an unique solution for the desired altitude. The fixed inlet boundary condition is applied to the thruster exit plane where the flow properties are mapped from a separate three-dimensional (3D) single-thruster solution, to ensure proper nozzle exhaust flow properties for the plume induced base environment calculations. The single-thruster, as seen in Fig. 3, has a circular cross-sectional chamber and transforms to a rectangular nozzle. The subsonic chamber inlet-flow properties were obtained from a thermo-equilibrium analysis[19] using engine conditions. This procedure of performing a separate thrust chamber calculation is important to the final solution[11] since the propulsive nozzle flow is the major source of the ensuing base-flow physics. For the base-bleed flow on the plug-base, a fixed inlet boundary condition is applied.

For convective heat transfer calculations, ambient temperature is prescribed as the forebody and aftbody surface temperatures, whereas 540 R is specified for all base surfaces per base-heating design convection. For radiation calculations, the surface emissivity of the entire vehicle is assumed to be 0.7.[12] The engine ramp is actively cooled and the surface temperature distribution is prescribed from a separate conjugate heat transfer calculation involving solid walls and coolant channel flows. It is found in this work that cowl-base irradiation is more than ten times higher if adiabatic condition is imposed on the ramp surface. Hence, a more accurate boundary condition is employed.

Results and Discussion

Two-dimensional (2D) Base-Heating Environment

Six 2D X-33 aerospike engine base flowfields are computed first and the operating conditions are shown in Table 2. The 2D computational domain is comprised of the aftbody, cowl base, thruster, engine ramp, plug base and plume expansion region (about 9 times the plug-base half-width). These cases essentially simulate a 2D cut of the 3D domain at the symmetry plane, without a realistic influence from the vehicle body flow. Nevertheless, these 2D computations provide valuable insight into the approximate base-flow physics with a fast turnaround time. Subsequently, these 2D solutions can be used with other engineering methods to predict a first-cut base-heating environment. For example, the 2D plume can be duplicated along the base and rotated at the end to construct a 3D pseudo-plume with which the irradiation to predetermined body points can be approximated. However, 3D base-heating effects such as the plume spillage, lateral wall jet impingement with the outer-base, and potential plume induced flow separation can not be acquired with a pseudo-plume method and have to be calculated with a true 3D vehicle-base-plume computation.

Table 2 Operating conditions

Case	PC/Pa	M_∞	h
1	63	0.00	0.7
2	92	0.60	3.7
3	158	0.98	7.7
4	510	1.72	15.3
5	1804	2.81	23.4
6	5790	4.07	31.1

Figure 4 shows a comparison of the predicted plug-base (flattened) convective heat fluxes. In Cases 1 and 2, the convective heat-flux of finite-rate chemistry is lower than that of frozen chemistry, due to the dissociation of H_2O. In general, the plug-base convective heat fluxes decrease with increasing altitudes until h = 7.7 km, above which the difference is not discernible - an indication of diminishing plume afterburning and air dilution (Case 3-6). That important finding leads to the frozen chemistry assumption in the 3D computation involving supersonic freestreams - a reduction of the participating species number from seven to a maximum of three (air, plume, and base-bleed). It is also found in 2D studies that local time-stepping can only be utilized in the initial stage to facilitate the solution development. Constant time steps must be followed to ensure synchronized time-marching to avoid false base flow-physics caused by biased local-flow residence time distribution.

3D Base-Heating Environment

Cases 2, 4, 5, and 6 from Table 2 were chosen for the 3D full-vehicle base environment computations. The 3D base flow physics such as the plume jumping on the cowl-base, plume spillage on the side-ramp, reverse jet impingement on the plug-base[1-2], and lateral wall-jet impingement on the outer- and offest outer-bases are highly three-dimensional and heavily depend on the incoming aftbody flow. Of particular interest is the outer- and offset outer-base heating due to the lateral wall-jet impingement since those are not actively cooled, and whether there is plume induced flow separation occurring at the highest altitude (Case 6). The formation of the reverse jet and the wall-jet (see Fig. 3) in linear aerospike engine base-flows is very similar to that of the multiple-nozzle clustered engine.[9-12]

The adequacy of the incoming flow is assessed by comparing the computed forebody and aftbody surface pressures with those of (limited) cold-flow wind tunnel test data. Figure 5 shows such a comparison at M = 0.60. The 7.75% scaled cold-flow test model had a slightly different ramp configuration and was running at lower nozzle pressure ratios. Nevertheless, the comparison is in general reasonable except for the aftbody region, where the cold-flow test shows a lower surface pressure than that of the flight simulations in which the progressive grid refinement seems to improve the comparison somewhat. This discrepancy is expected since in subsonic flow environment, the aftbody surface pressure is affected by variations in ramp configuration, jet molecular weight, and NPR. In addition, the cold jets tend to produce higher drag[20] - a higher entrainment that tends to accelerate the flow over the aftbody resulting in a decrease in the aftbody surface pressure. In supersonic freestreams, the signal from the propulsive plume does not transmit forward and the comparison of surface pressures for M = 1.72 computation with those of the cold-flow test at $M = 1.60$ and $M = 1.80$ is excellent, as shown in Fig. 6. These comparisons indicate that the incoming flow environment is adequately simulated for base flow development.

Figure 7 shows the comparison of base pressure characteristic curves, i.e., the distribution of the base-center pressure as a function of ambient pressure.[10] The general trend of the cold flow base-center pressure is lower than that of the model flight predictions - an agreement with the intuition and observation[11] that base pressure of hot flow is higher than that of the cold flow. In 2D predictions, the dissociation of water in the base region resulted in lower base temperatures and pressures for the finite-rate chemistry case than those of the frozen chemistry case. In 3D predictions without base-bleed, the base pressures are generally lower that those of the 2D predictions. That trend is reasonable since the 3D computation allows the plume spillage and lateral wall-jet formation and therefore weaker reverse jet impingement, whereas the 2D calculation precludes either physics. In 3D predictions with base-bleed, the effect is to increase the base-center pressure, except at $PC/Pa = 5790$ where the effect is much diluted due to the highest plume expansion. The combined characteristic curves of the cold-flow test and flight prediction (without base-bleed) also show that the base wake closes - when base-center pressure is not changed by the ambient pressure - at a pressure ratio of approximately 500. The discussion of Fig. 7 indicates the base pressure characteristic curves predicted by the current model are reasonable.

Figure 8 shows the computed full-vehicle convective heat-flux contours without base-bleed, with emphasis on the vehicle-base side. Different scales are used for different regions such that the flow physics can be revealed. Unique base heat flux patterns are formed in each case due to the interaction of the reverse jet and the lateral wall-jet with the pillowed plug-base, and that of the lateral wall-jet with the outer-base and offset outer-base. The highest heat-flux level occurs at the inlet of the ramp surface where it is just downstream of the "throat" of an equivalent unexposed nozzle. The ramp-side plume spills over the ramp side-wall, causing increased heat-flux level at the boundary. In general, the plug-base convective heat-flux decreases with increasing altitudes - the result of an attenuating reverse jet, whereas the outer- and offset outer-base convective heat fluxes increase with increasing altitudes - an indication of stronger lateral wall jet impingement. The level of the heat fluxes on the inner- and outer-bases, however, is less than that of the plug-base and much less than that of the engine ramp. When the base-bleed is turned on, it is assumed that the entire base-bleed region is covered with a protective layer of bleed-gas. As a result, the bleed region is lumped as an inlet boundary and the convective heat-flux to the bleed region is assumed to be zero. The convective heating to the rest of the plug-base can be computed and is generally lower due to the expansion of the base-bleed. At 2% base-bleed, the convective heat-flux contours (not shown) on the rest of the bases are very similar to those in Fig. 8.

Figure 9 shows the computed radiative heat-flux contours without base-bleed. The characteristics of the computed radiative heat-flux contours look dissimilar to those of the convection (Figs 8). The convective heating is transported through direct contact of the propulsive flow with the solid surface, whereas the radiative heating is transported through view factors. For example, in Case 2 (3.7 km) of Fig. 9, the inner side of the vertical fin exhibits the effect of the radiative heating but not the convective heating (Fig. 8). In addition, the top and bottom parts of the inner- and outer- bases show effects of radiative heating but not the middle section, indicating the view from most of the plume is blocked by the nozzle plug in the near field. Again, the computed radiative heat-flux contours with base-bleed (not shown) is very similar to those without base-bleed except for the plug-base region. Unlike the convective heat- flux, the lowered radiative heat-flux to the plug-base due to base-bleed can be computed since the bleed inlet can be treated as a solid wall in radiation calculations. The plug-base radiative heat-flux reduction due to base-bleed is computed as from approximately 150 to 200 kW/m^2. Notice the ramp surface temperature is prescribed with a separate conjugate heat transfer calculation and the effect of surface radiation is included in all the calculations. This is another improvement over the conventional plume radiation calculation in which the surface radiation is not included.

The total plume induced base-heating is the combination of both modes: convection and radiation. Figure 10 shows the total base-heat fluxes along the horizontal base centerline without base-bleed, whereas Fig. 11 shows those with base-bleed. The abscissa is a wetted distance starting from the geometrical center of the plug-base, moving right or left along the centerline longitudinally, turning and dropping down the ramp side-wall, crossing the inner-base, up the off-set outer-base, moving along the outer-base and ending at the side of vehicle. In these figures, the plug-base is subjected to the most heating and the base-bleed helps to relieve some of that heating. In general, the total heating impressed upon the plug-base decreases with altitude, whereas the total heating imposed on the other bases increases with altitude, due to the strengthening of the lateral wall jet.

Plume-induced flow separation (PIFS) at high altitudes is normally not a heating concern unless recirculated base region exhaust flows are drawn into the PIFS region and burning occurs (as was the case for the Saturn V). Although PIFS for Saturn V reportedly started at about 24 km,[21] it is anticipated that the historical PIFS database for conventional launch vehicles may not be applicable to the X-33. As it turned out, PIFS is not observed for any of the test cases performed in this study, even in Case 6 at 31.1 km. A good explanation is attributed to the altitude compensating effect of the aerospike plume that limited the plume expansion angle. In addition, the shape of the "flying wedge" is such that the total base area is large and the cowl-, inner-, offset outer- and outer-base pressures do not rise enough to help communicate upstream through the surface boundary layer, as do the conventional engine and base designs. Only the plug-base has a more significant pressure rise due to the reverse-jet impingement, but it is too far away from the aftbody and vented out by the lateral wall-jet, resulting in a almost constant base pressure characteristic curve at high altitudes, as shown in Fig. 2. Furthermore, the direction of the lateral wall-jet is perpendicular to the major axis of the aftbody, further reduces the chance of a PIFS.

Conclusion

A computational methodology is developed to study the 3D linear aerospike engine plume induced X-33 base-heating environment. Three grid distribution methods are utilized to minimize the grid requirement of a full-vehicle thermo-flowfield computation: solution-adaptive, patched, and embedded grid schemes. The effects of 3D base-flow physics such as plume jumping, plume spillage, plug-base reverse jet formation, and plug-base lateral wall jet impingement with the inner- and outer-base surfaces are captured and reflected in the computed base-heating environment. The base-heating reduction effect of base-bleed and the potential for plume-induced flow separation are studied. The result contributed to the X-33 base thermal protection system design and the methodology and procedures developed represent an improvement in the base-heating design area over the conventional methods in several aspects.

Acknowledgment

This work was performed under the cooperative agreement between Lockheed Martin Skunk Works and NASA MSFC for the Phase II Reusable Launch Vehicle/X-33 Technology Development Program. Patrick Rodi of LMSW is the base-heating project lead and Mark Seaford is the MSFC task lead. Robert Williams provided the baseline 3D grid and Joni Cornellison generated the refined 3D engine ramp and pillowed plug-base grids. Mark D'Agostino provided the cold flow wind tunnel test data. The patched- and embedded-grid formulations were developed by Engineering Sciences, Inc. under a separate "Injector Design Tool Improvements" contract (NAS8-40582).

References

[1] Huang, D.H., "Aerospike Engine Technology Demonstration for Space Propulsion," AIAA Paper 74-1080, Oct. 1974.

[2] Lamont, E.A., "The Aerospike Engine System for the Space Tug - A Status Report," AIAA Paper 73-1245.

[3] Steinbrenner, J.P., Chawner, J.R., and Pouts, C., "Multiple Block Grid Generation in the interactive Environment," AIAA Paper 90-1602, June 1990.

[4] Davies, C.B., and Venkatapathy, E., "The Multidimensional Self-Adaptive Grid Code, SAGEv2," NASA TM 110350, April 1995.

[5] Chen, Y.-S., "FDNS - A General Purpose CFD Code, Version 4.0," Engineering Sciences, Inc., ESI-TR-97-01, Huntsville, AL, May 1997.

[6] Liu, J., Shang, H.-M., Chen, Y.-S., and Wang, T.-S., "GRASP: A general Radiation Simulation Program," AIAA Paper 97-2559, June, 1997.

[7] Wang, T.-S., and Luong, V., "Hot-Gas-Side and Coolant-Side Heat Transfer in Liquid Rocket Engine Combustors," *Journal of Thermophysics and Heat Transfer*, Vol. 8, No. 3, 1994, pp. 524-530.

[8] Wang, T.-S., and Chyu, M.K., "Heat Convection in a 180-Deg Turning Duct with Different Turn Configurations," *Journal of Thermophysics and Heat Transfer*, Vol. 8, No. 3, 1994, pp. 596-601.

[9] Wang, T.-S., "Numerical Analysis of Base Flowfield for a Four-Engine Clustered Nozzle Configuration," *Journal of Propulsion and Power*, Vol. 11, No. 5, 1995, pp. 1076-1078.

[10] Wang, T.-S., "Grid-Resolved Analysis of Base Flowfield for Four-Engine Clustered Nozzle Configuration," *Journal of Spacecraft and Rockets*, Vol. 33, No. 1, 1996, pp. 22-29.

[11] Wang, T.-S., and Cornelison, J., "Analysis of Flowfields over Four-Engine DC-X Rockets," *Journal of Spacecraft and Rockets*, Vol. 34, No. 5, 1997, pp. 620-627.

[12] Wang, T.-S., "Delta Clipper-Experimental In-Ground Effect on Base-Heating Environment," *Journal of Thermophysics and Heat Transfer*, Vol. 12, No. 2, 1998.

[13] Wang, T.-S., and Chen, Y.-S., "Unified Navier-Stokes Flowfield and Performance Analysis of Liquid Rocket Engines," *Journal of Propulsion and Power*, Vol. 9, No. 5, 1993, pp. 678-685.

[14] Chen, Y.-S., and Kim, S. W., "Computation of Turbulent Flows Using an Extended k-ε Turbulence Closure Model," NASA CR-179204, Oct. 1987.

[15] Wang, T.-S., McConnaughey, P., Chen, Y.-S., and Warsi, S., "Computational Pollutant Environment Assessment from Propulsion System Testing," *Journal of Spacecraft and Rockets*, Vol. 33, No. 3, 1996, pp. 386-392.

[16] Liakopolous, A., "Explicit Representations of the Complete Velocity Profile in a Turbulent Boundary Layer,"*AIAA Journal*, Vol. 22, No. 6, 1984, pp. 844-846.

[17] White, F.M., *Viscous Fluid Flow*, McGraw-Hill, New York, 1974.

[18] Liu, J., Shang, H.-M., Chen, Y.-S., and Wang, T.-S., "Prediction of Radiative Transfer in General Body-Fitted Coordinates," *Numerical Heat* Transfer, Part B, Vol. 31, 1997, pp. 423-439.

[19] Svehla, R.A., and McBride, B.J., "FORTRAN IV Computer Program for Calculation of Thermodynamic and Transport Properties of Complex Chemical Systems," NASA TN D-7056, Jan. 1973.

[20] Peters, W.L., "A Comparison of Jet Temperature Effects on Afterbody Drag with Those from Jet Molecular Weight and Nozzle Area Ratio Variations," AIAA Paper 80-1161.

[21] Wilkinson, C.L., "Heat Transfer Within Plume-Induced Flow Separation Regio on Saturn V," ASME Paper No. 69-WA/HT-18, November 1969.

List of Figure Captions

Fig. 1 Layout of an X-33 surface computational grid.

Fig. 2 Grid distribution of a solution-adapted symmetry plane with zonal outlines.

Fig. 3 Layout of the cowl-base, 40-thruster engine, ramp and pillowed plug-base assembly.

Fig. 4 Comparison of the 2D computation predicted plug-base convective heat fluxes.

Fig. 5 Comparison of the forebody and aftbody surface pressure coefficients (Case 2).

Fig. 6 Comparison of the forebody and aftbody surface pressure coefficients (Case 4).

Fig. 7 Comparison of base pressure characteristic curves.

Fig. 8 Convective heat flux contours without base-bleed for Cases 2, 4, 5, and 6 in three scales: ramp, 0-9000; plug-base, 0-400; and the rest, 0-60.

Fig. 9 Radiative heat flux contours without base-bleed for Cases 2, 4, 5, and 6 in three scales: ramp and cowl-base, 0-625; plug-base, 0-400; and the rest, 0-170.

Fig. 10 Base horizontal centerline total heat fluxes without base-bleed.

Fig. 11 Base horizontal centerline total heat fluxes with base-bleed.

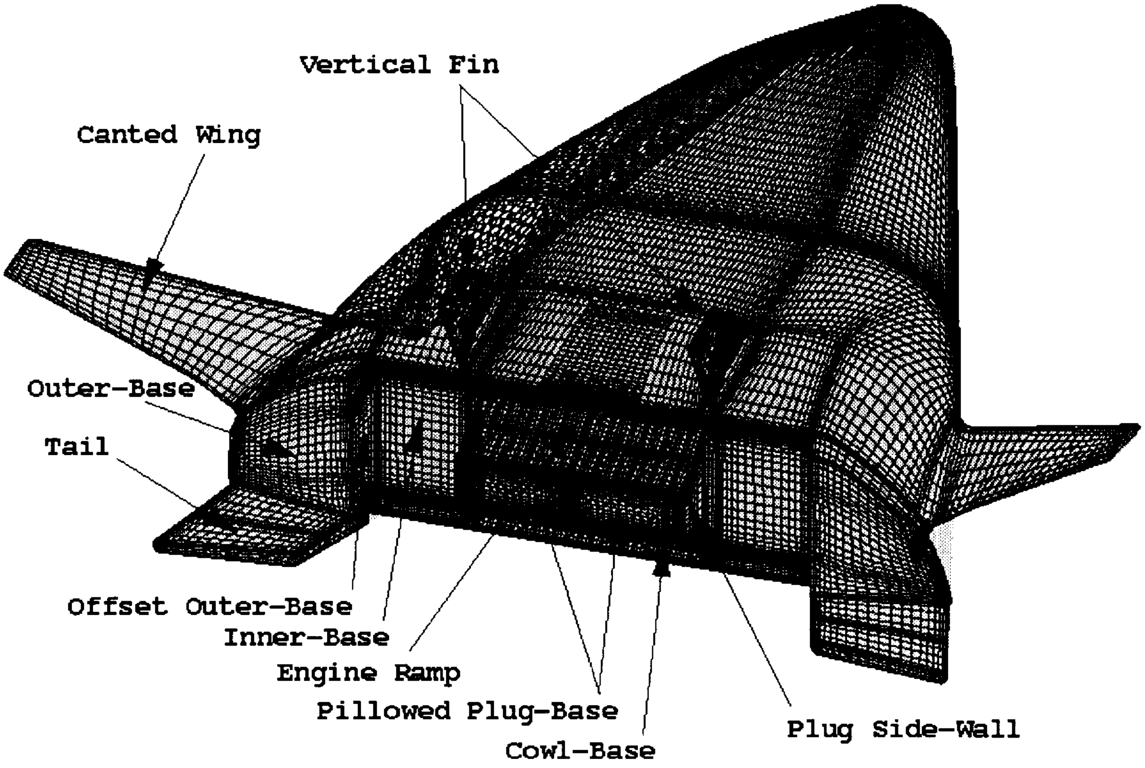

Fig. 1 Layout of an X-33 surface computational grid.

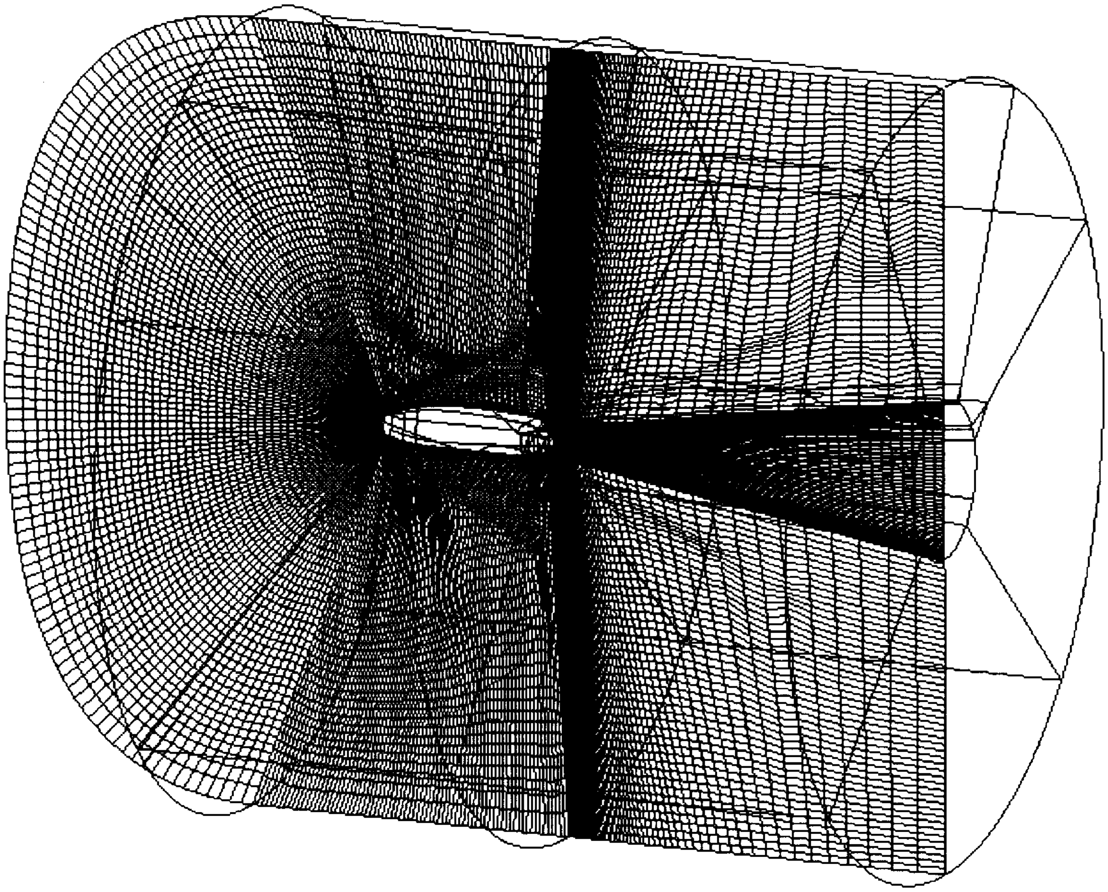

Fig. 2 Grid distribution of a solution-adapted symmetry plane with zonal outlines.

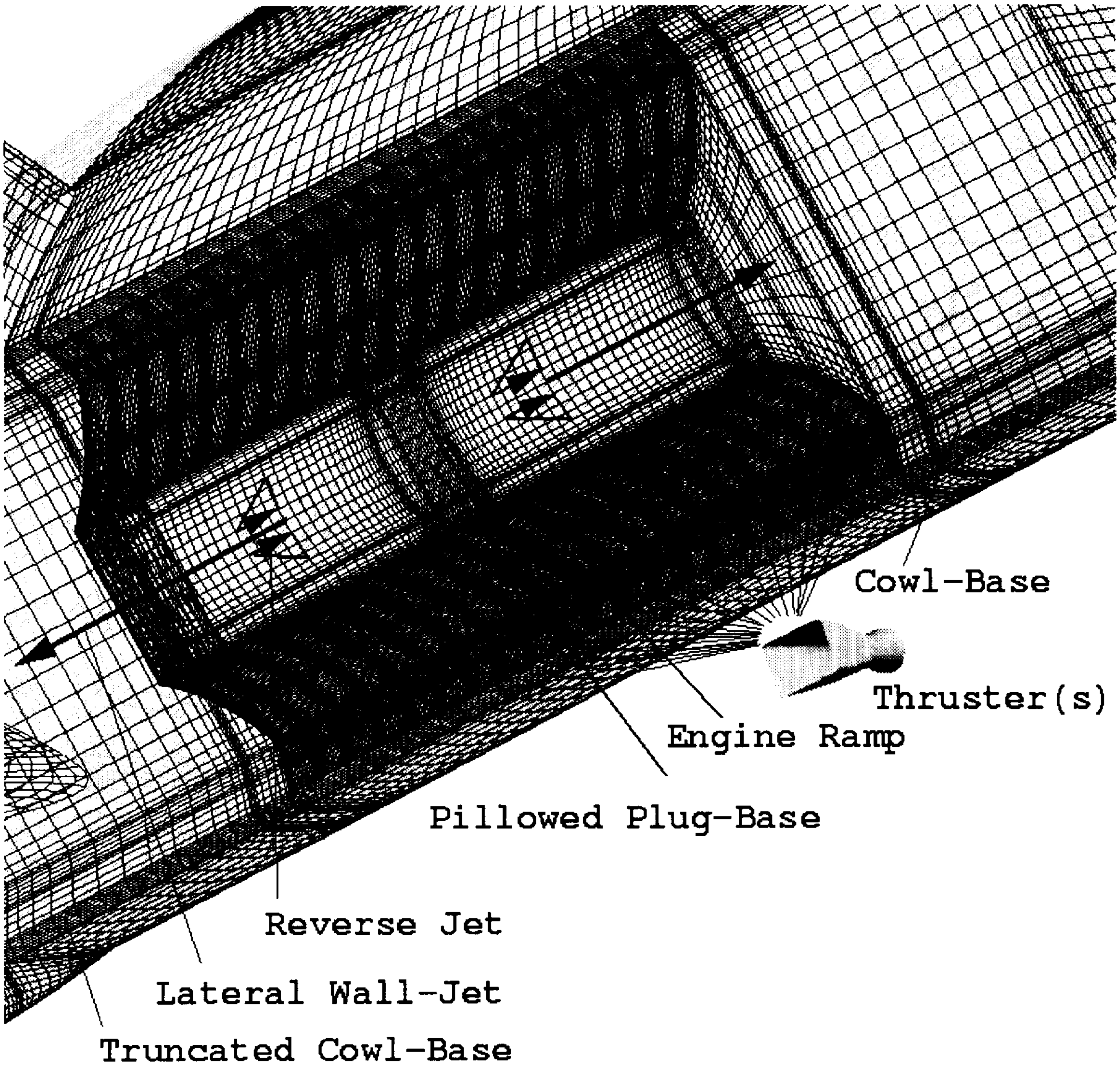

Fig. 3 Layout of the cowl base, 40-thruster engine, ramp, and pillowed plug-base assembly.

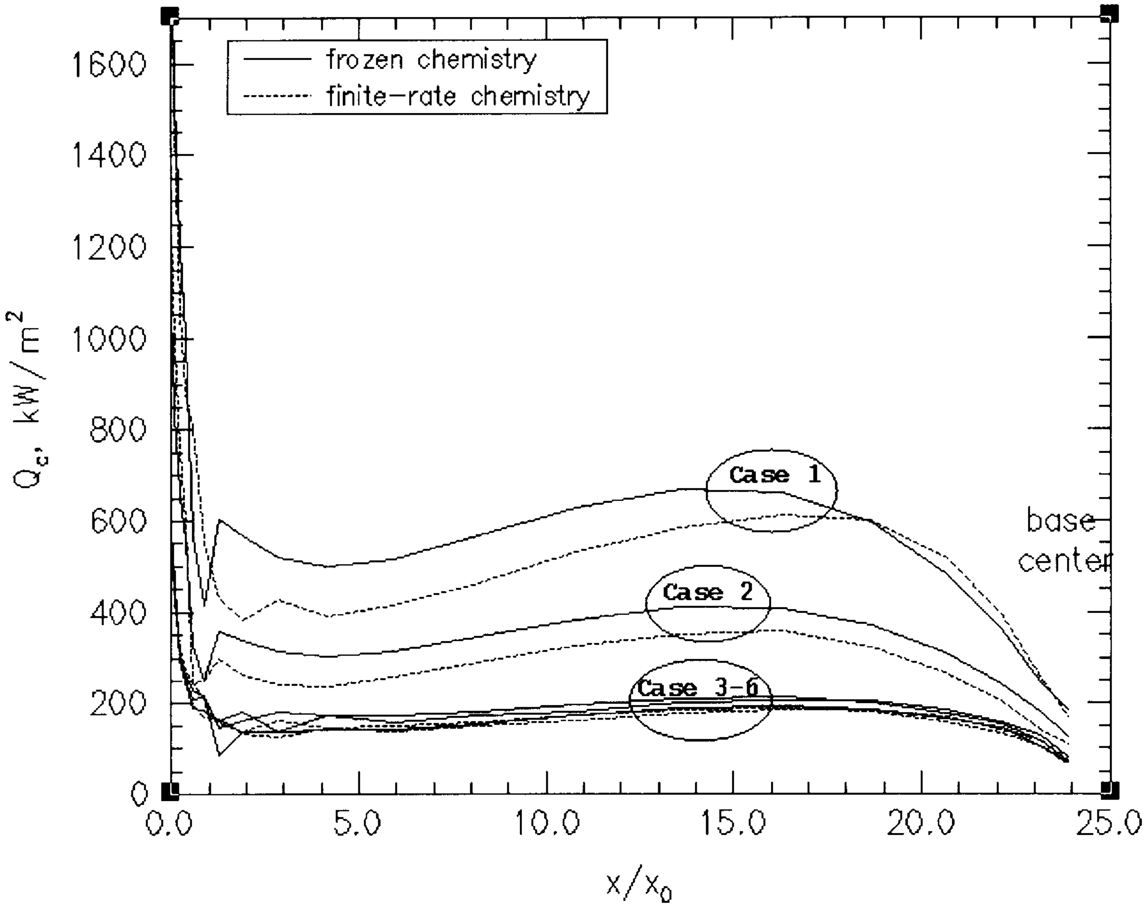

Fig. 4 Comparison of the 2D computation predicted plug-base convective heat fluxes.

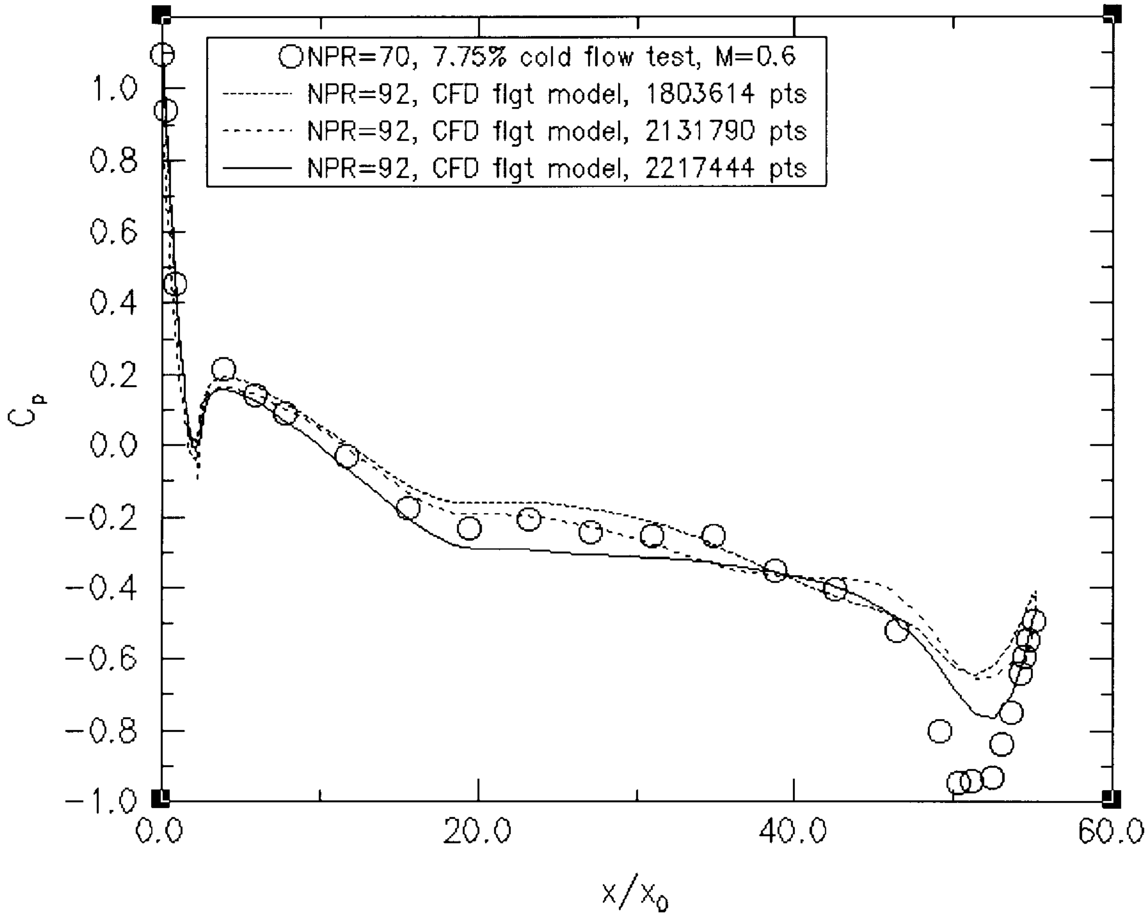

Fig. 5 Comparison of the forebody and aftbody surface pressure coefficients (Case 2).

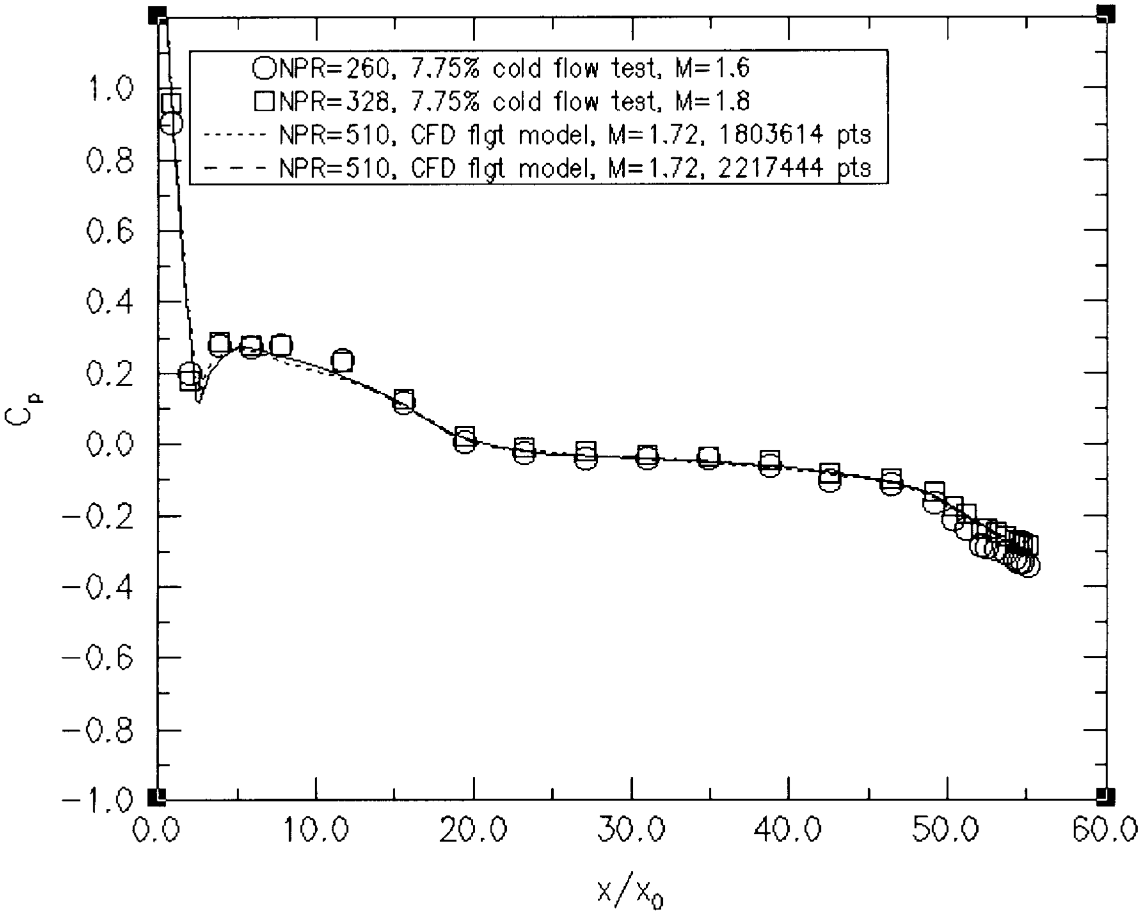

Fig. 6 Comparison of the forebody and aftbody surface pressure coefficients (Case 4).

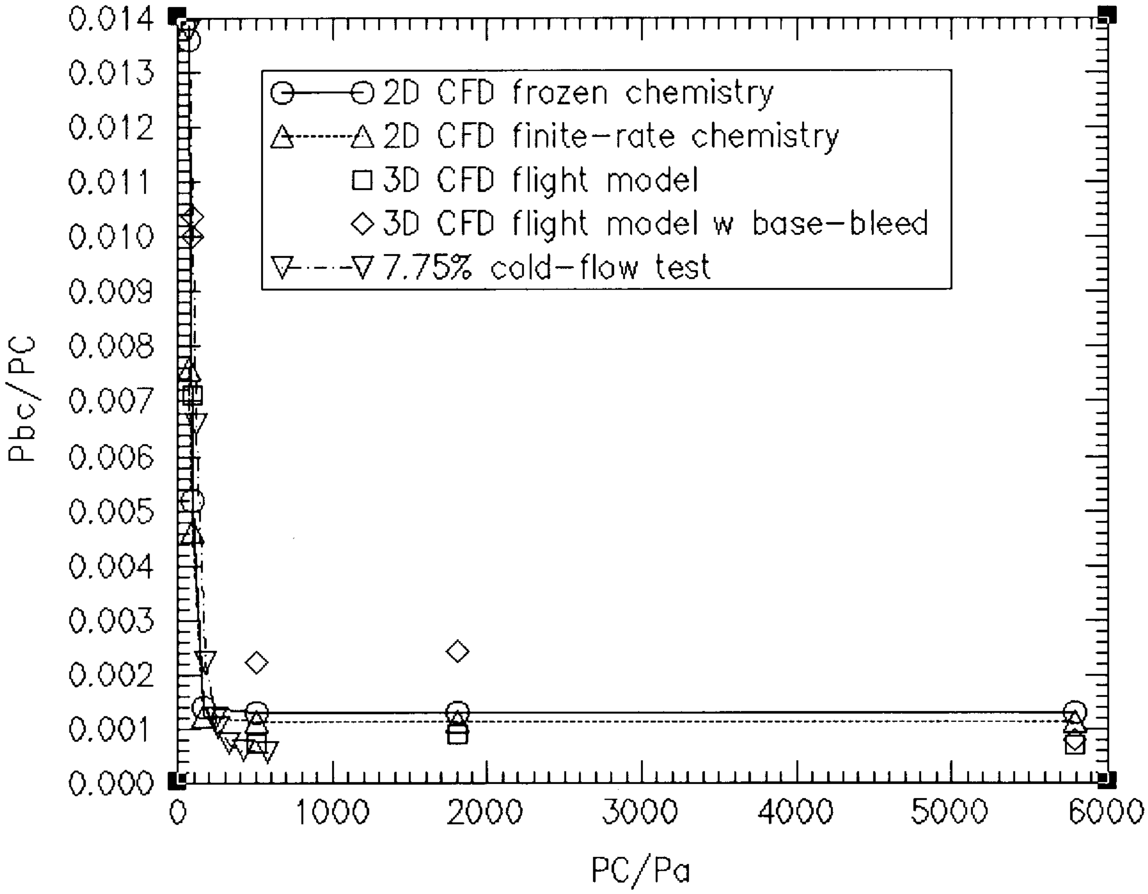

Fig. 7 Comparison of base pressure characteristic curves.

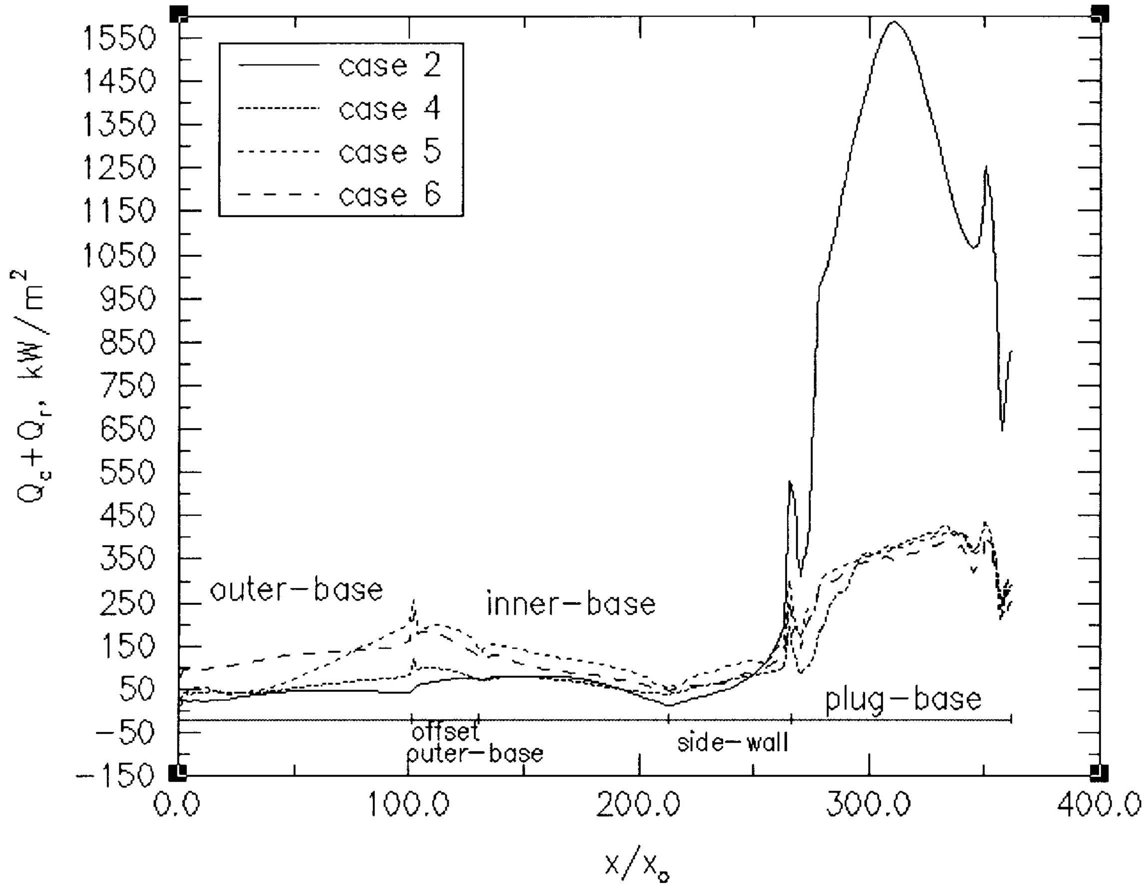

Fig. 10 Base horizontal centerline total heat fluxes without base-bleed.

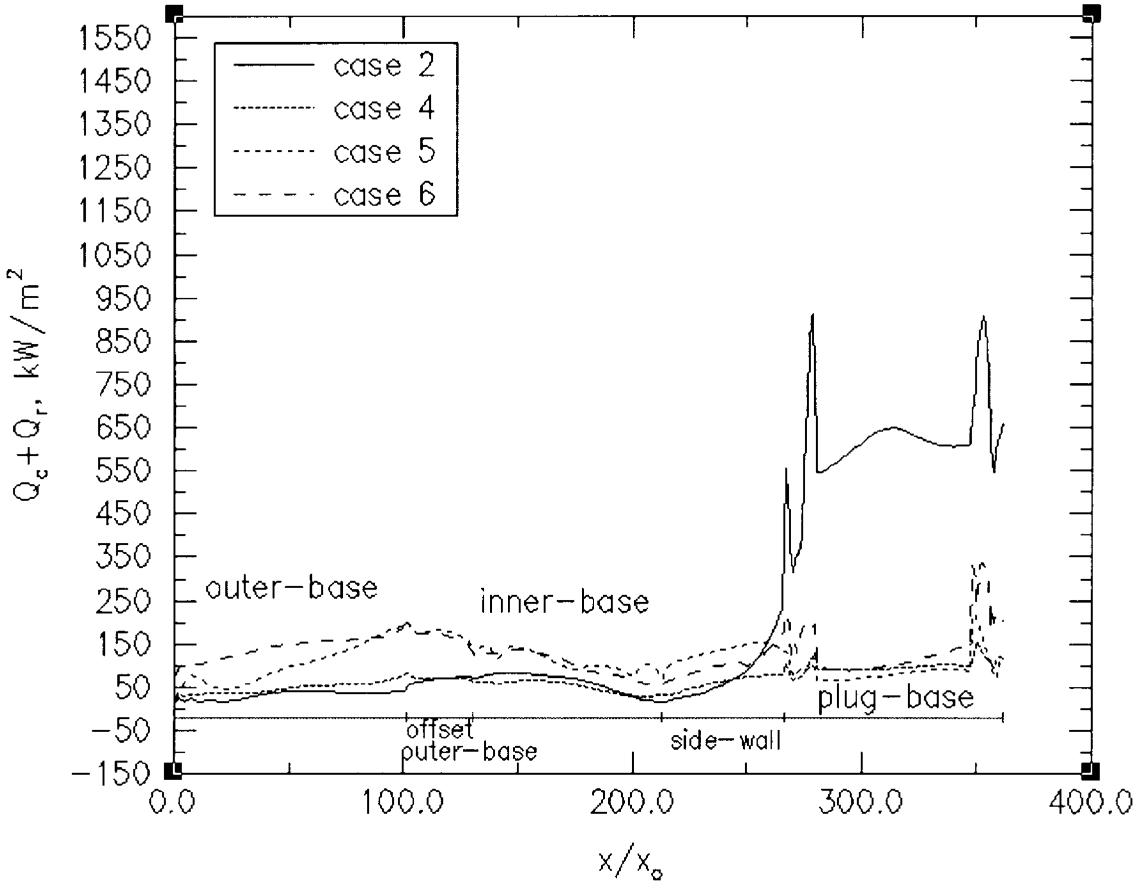

Fig. 11 Base horizontal centerline total heat fluxes with base-bleed.